Journal of Energy Chemistry 64 (2022) 520–530

Contents lists available at ScienceDirect

Journal of Energy Chemistry

journal homepage: www.elsevier.com/locate/jechem

http://www.journals.elsevier.com/journal-of-energy-chemistry/

Monitoring dynamics of defects and single Fe atoms in N-functionalized few-layer graphene by in situ temperature programmed scanning transmission electron microscopy

Rosa Arrigo [a,b,*], Takeo Sasaki [c], June Callison [d,e], Diego Gianolio [b], Manfred Erwin Schuster [f,*]

[a] School of Science, Engineering and Environment, University of Salford, Manchester M5 4WT, UK
[b] Diamond Light Source, Harwell Science and Innovation Campus, Didcot OX11 0DE, UK
[c] JEOL UK Ltd. JEOL House, 1-2 Silver Court, Watchmead, Welwyn Garden City, Herts AL7 1LT, UK
[d] Department of Chemistry, University College London, 20 Gordon Street, London WC1H 0AJ, UK
[e] UK Catalysis Hub, Research Complex at Harwell (RCaH), Rutherford Appleton Laboratory, Harwell Oxon OX11 0FA, UK
[f] Johnson Matthey Technology Centre, Reading RG4 9NH, UK

ARTICLE INFO

Article history:
Received 27 November 2020
Revised 6 May 2021
Accepted 7 May 2021
Available online 18 May 2021

Keywords:
HAADF-STEM
Single Fe atom sites
N-doped
Few-layer graphene
Dinuclear Fe species

ABSTRACT

In this study, we aim to contribute an understanding of the pathway of formation of Fe species during top-down synthesis of dispersed Fe on N-functionalized few layer graphene, widely used in electrocatalysis. We use X-ray absorption spectroscopy to determine the electronic structure and coordination geometry of the Fe species and *in situ* high angle annular dark field scanning transmission electron microscopy combined with atomic resolved electron energy loss spectroscopy to localize these, identify their chemical configuration and monitor their dynamics during thermal annealing. We show the high mobility of peripheral Fe atoms, first diffusing rapidly at the trims of the graphene layers and at temperatures as high as 573 K, diffusing from the edge planes towards in-plane locations of the graphene layers forming three-, four-coordinated metal sites and more complexes polynuclear Fe species. This process occurs via bond C-C breaking which partially reduces the extension of the graphene domains. However, the vast majority of Fe is segregated as a metal phase. This dynamic interconversion depends on the structural details of the surrounding graphitic environment in which these are formed as well as the Fe loading. N species appear stabilizing isolated and polynuclear Fe species even at temperatures as high as 873 K. The significance of our results lies on the fact that single Fe atoms in graphene are highly mobile and therefore a structural description of the electroactive sites as such is insufficient and more complex species might be more relevant, especially in the case of multielectron transfer reactions. Here we provide the experimental evidence of the formation of these polynuclear Fe–N sites and their structural characteristics.
© 2021 Science Press and Dalian Institute of Chemical Physics, Chinese Academy of Sciences. Published by ELSEVIER B.V. and Science Press. All rights reserved. This is an open access article under the CC BY license (http://creativecommons.org/licenses/by/4.0/).

1. Introduction

In the field of electrocatalysis, graphitic supports are largely used as redox-active materials [1]. Edge terminations and in-plane point defects, such as non 6-membered rings and vacancies on the basal planes of the graphene layers induce localized charge accumulation or depletion [2], accounting for the reactivity of graphitic carbon materials in acid/base catalysis, redox catalysis and electrocatalysis [3–7]. Edges and vacancies in graphitic carbon materials are often terminated not only by H atoms but also other heteroatoms, such as O, N, B and P, and these sites have been exploited for anchoring metal active species [8–10]. The nature of the defects in different carbon materials has been extensively described, including a recent comprehensive review on the structural defects typifying various forms of carbon materials and their influence on the catalytic activity and selectivity of metal nanoparticles immobilized on these. [11] Examples of point defects in the graphene layers are single vacancy, 5-8-5 and 555-777 divacancy structures, Stone Wales (5775) defects. These defects can also contain heteroatoms in various configuration; in the case of N-species these include graphitic, pyridinic, and pyrrolic nitrogen [12]. These

* Corresponding authors at: School of Science, Engineering and Environment, University of Salford, Manchester M5 4WT, UK (Rosa Arrigo); Johnson Matthey Technology Centre, Reading RG4 9NH, UK (Manfred Erwin Schuster).
E-mail addresses: r.arrigo@salford.ac.uk (R. Arrigo), manfred.schuster@matthey.com (M.E. Schuster).

https://doi.org/10.1016/j.jechem.2021.05.005
2095-4956/© 2021 Science Press and Dalian Institute of Chemical Physics, Chinese Academy of Sciences. Published by ELSEVIER B.V. and Science Press. All rights reserved. This is an open access article under the CC BY license (http://creativecommons.org/licenses/by/4.0/).

defects interact with the metal species in a different way and with various strength enabling chemical tunability of the physico-chemical properties [13,14]. In this contribution we are concerned with the detailed structural analysis of Fe species on N-functionalized nanocarbons widely investigated as alternative to platinum group metals systems in electro-catalytic applications such as the oxygen reduction reaction (ORR) [15], the electrochemical CO_2 reduction [16,17] and the electrochemical NH_3 synthesis [18].

Of interest, low nuclearity Fe species interacting with highly graphitic carbon via a direct coordination to N atoms emerged in our previous contribution as relevant sites for the electrochemical activation and conversion of CO_2 into C2 products [17].

Operando X-ray absorption spectroscopy provided evidence for *in situ* generated Fe(II) species on N-doped graphite, whereas only metallic Fe forms on the N-free counterpart under the same polarization conditions. We note that diluted bi-carbonated solution can assist the mobilization of Fe(III) via reduction to Fe(II) [17], however the applied potential for the CO_2RR was sufficiently low for the total reduction of Fe(III) to metal which occurs already at $E^0_{Fe3+/Fe0} = -0.204$ V vs Ag/AgCl. Ligands effect can influence the thermodynamic redox potential of a redox couple and therefore, the experimental observation for Fe–N systems can be explained by invoking the participation of the N-ligands of the support to stabilize in situ generated active Fe(II) species. The appealing selectivity observed and the poor stability that these systems suffer, all together generates a pressing quest for understanding at the molecular level the structure of the defects containing electroactive metal atoms in graphitic carbon materials and their transformation into a metallic phase if sufficient energy is provided. This knowledge is of paramount to meliorate their design towards more stable electrocatalysts, especially considering that the total reduction of Fe cations to metallic Fe is accompanied by an increase of the parasitic hydrogen evolution [17]. With the advent of atom resolving transmission electron microscopes (TEM), a plethora of contributions have unveiled the existence of single atom sites, paving the way towards the recognition and the raise of single atom catalysis (SAC) [19–26]. Aberration corrected TEM in combination with density functional theory was used to investigate in situ generated Fe metal atoms in graphene vacancies [24]. Dynamics of bonding breaking and making leading to the formation of various in-plane single metal atoms, tri and four coordinated to C atoms, were described therein. These are similar to the Fe–N_4 ensembles, with either pyrrolic- or pyridine-like N species coordinated to Fe, suggested as active sites for the electrocatalytic oxygen reduction reaction [27]. However, it is expected that N-doped graphene-based electrode materials produced via wet and thermal chemistry routes might present a more complex metal speciation, rationalizing the C–C coupling activity of these systems [17].

Motivated by this reasoning, we undertook a high angle annular dark field scanning transmission electron microscopy (HAADF-STEM) study in combination with X-ray absorption spectroscopy (XAS) with the aim to identify the nature of the defects initially present on N-doped few-layers graphene (NFLG) and the localization as well as the nature of the Fe species formed upon adsorption on the NFLG from an Fe(II) aqueous solution. Furthermore, we study the behavior of these two systems upon *in situ* annealing by means of HAADF-STEM as a way to simulate commonly applied thermal post treatment following Fe immobilization, and clarify the transformations of these into other forms as a function of temperature. We use aberration corrected HAADF-STEM which enables generating images with contrast proportional to the square of the atomic number of the visualized atoms and therefore particularly useful to localize heavy elements with atomic resolution on supports composed of light-elements such as C materials [5]. Moreover, we use atomic resolved energy loss electron spectroscopy (EELS) to identify the local elemental composition of selected Fe ensembles. Not only this study allows us to identify the various species formed during the thermal annealing step of the synthetic protocol, but also to draw some parallels for identifying the structural dynamics responsible for the degradation of the catalytic performances. Even if the dynamics presented here are related to the specific conditions realized in our experiments, the degradation path is found to be similar to the one observed under electrochemical condition [17], which corroborate the significance of our results. The metal sites identified in our study can be used as models for theoretical approaches for the analysis of electrocatalytic reaction mechanisms.

2. Experimental

2.1. Sample preparation

Graphene oxide in powder form with 4–10% edge oxidized (796034-1G, Sigma-Aldrich, UK) was functionalized with N following a procedure previously reported [28]. Accordingly, 0.6 g of graphene oxide was added to a ceramic boat and placed in a quartz tube furnace. The tube was placed in a Carbolite MTF 10/25/130 furnace and helium gas (BOC, 99.996%) was flowed through the system at a rate of 50 ml/min to purge the sample for 30 min. The gas flow was switched to ammonia (99.98% Ammonia Micrographic, BOC Linde) and the sample heated to 873 K at a ramp rate of 10 K/min and then held at this temperature for 4 h. Afterwards the sample was cooled down to 313 K in NH_3 and further to room temperature in He (50 mL min^{-1}, BOC Linde) and transferred to a glass vial. This sample is referred to as NFLG. Fe was immobilized on NFLG via ionic exchange. Accordingly, 1 g/L aqueous solution of ferrous ammonium sulfate hexahydrate (99% Merk) was prepared . 16 mg of NFLG were suspended in 20 mL of the Fe containing aqueous solution to which also 1 mL of pure ethanol was the added. The suspension was left to exchange for 2 h at room temperature. Subsequently the suspension was vacuum filtered and rinsed once with distilled water. The solid was left to dry at room temperature in a desiccator until used for characterization. This sample is referred here as Fe/NFLG. The few layers graphene (FLG) sample used as reference for EXAFS analysis was obtained from the commercial graphene oxide using the same procedure as for NFLG expect that only He is used instead of NH_3.

2.2. X-ray absorption spectroscopy

XAS data were collected at B18 beamline at Diamond Light Source at the Fe K-edge (7112 eV) using Pt-coated mirrors, a Si111 monochromator and harmonic rejection mirrors to remove higher harmonics. The samples, in powder form, were first deposited onto a substrate, covered with Kapton tape and then measured. The data were collected in fluorescence mode using a 36-element solid state Ge detector positioned at 90° with respect to the incoming beam. The spectra were normalized to the I_0 signal measured by an ion chamber placed before the sample and filled with ca. 250 mbar of N_2 and up to 1 atm He, resulting in an absorption of ca 7% of the incoming beam. For the Fe K edge X-ray absorption near edge spectroscopy (XANES) measurements, the energy was scanned from 6912 to 8112 eV (k-range up to 16 $Å^{-1}$) with a constant energy step of 0.3 eV and a total acquisition time of ca. 4 min per scan. Between 20 and 40 scans were measured for each sample and then averaged to achieve a good signal to noise ratio; the actual number depending on the Fe concentration.

Data processing and analysis were performed with Athena and Artemis software from Demeter package using IFEFFIT code [29]. The fits of the Fourier Transform extended X-ray absorption fine

structure (FT-EXAFS) spectra were performed in k-range from 2.5 to 12.5 $Å^{-1}$ and R-range from 1 to 2 Å if only the first shell was fitted for NFLG and from 1 to 3.4 Å if also the second shell was included for the Fe/NFLG. The reference sample for the non-metallic phase of NFLG, that is FLG, was fitted by fixing the coordination number to 5 and using a single scattering path for Fe-ligand (Fe-L) to simulate first shell signal. NFLG was fitted with two paths for first shell fixing the amplitude to same value obtained by best fit of FLG scaled by a factor 0.625 which is the percentage of atoms in a non-metallic state as obtained by linear combination fit (LCF) of XANES data. Whilst amplitude was fixed, the coordination numbers for the two paths were left unconstrained and resulted in 4.1 and 1.9 for the two paths, consistent with a total coordination number of 6. The ΔE and Debye-Waller factor for Fe–L scattering were also constrained to the values obtained for FLG. Four paths were used for the fit of Fe/NFLG, two Fe–L for first shell and two Fe–Fe for second shell. Similarly, the amplitude was constrained and the coordination numbers was optimized by the fit.

2.3. HAADF-STEM and EELS

TEM analysis was carried out using a JEOL ARM200F cold field FEG probe corrected electron microscope operated at 80 keV to stay below the knock-on damage threshold for carbon [24]. Bright field (BF) and HAADF-STEM micrographs were acquired with a beam current of 4.2 pA and detector collection angles of 32.4–110.7 mrad and 0–18.9 mrad, respectively. STEM electron energy loss spectroscopy (EELS) spectrum image (SI) line scans were acquired using a GATAN Quantum ER dual EELS system using a collection half angle of 94.3 mrad, a probe convergence semi-angle of 30.5 mrad and a beam current of 15.4 pA. The quantitative analysis of C, N and Fe was obtained from EELS measurements at the CK, NK and Fe L edges with the signal being extracted from individual pixels (0.056 nm step size) as well as integrating over 2 pixels (0.112 nm) in the EELS line scans as indicated in the specific case.

The sample was drop casted onto a DENS solutions in-situ heater chips and the in-situ heating experiment was carried out with a DENS solutions wildfire double tilt heating holder. A 10 K/min heating ramp up to 1073 K was used with holding points at 373, 573, 773, 973 and 1073 K for data acquisition.

2.4. X-ray photoelectron spectroscopy

X-ray photoelectron spectroscopy (XPS) at the N 1*s* core level was performed at the VERSOX beamline of the DLS synchrotron facility [30] using X-ray excitation energy corresponding to a kinetic energy (KE) of 450 eV and an energy pass Ep of the analyzer set to 20 eV. The core level envelope was fitted using Casa XPS software after subtraction of a Shirley background and using a fitting model reported in Refs. [8,14].

2.5. Energy dispersive X-ray spectroscopy

Energy dispersive X-ray spectroscopy (EDX) analysis was performed on a JSM-6610LV scanning electron microscope (JEOL) fitted with Oxford Instruments Xmax 80 mm EDX detector. The samples were dispersed on a conductive carbon tab placed on an aluminum stub. The acceleration voltage was 10 kV.

3. Results and discussion

3.1. Elemental composition and Fe speciation of NFLG and Fe/NFLG

Herein, we investigate NFLG and Fe-NFLG derived from commercial few layer graphene oxide. The elemental composition of these samples and the starting graphene oxide is reported in Table S1. Accordingly, the starting graphene oxide presents impurities consisting of Fe, Si, Na, Ca in very small amounts and not homogeneously distributed in the sample. As expected, small quantities of impurities are also found on the samples NFLG, whereas the addition of Fe via ionic exchange allows a considerable higher loaded sample. In this case a rather homogeneous distribution of Fe is found amounting to 7.57 ± 0.80 in weight percent. This is much higher that the amount of N, indicating that: a) Fe interacts also with other sites in NFLG; b) olation and oxolation reactions take place leading to polynuclear species. Following, we are able to confirm the latter hypothesis. The quantitative elemental analysis of the surface of this sample as determined by XPS analysis with probing depth corresponding to ~0.5 nm indicates an atomic composition of 28% O, 6% N, 28% Fe and 38% C, suggesting that O is the predominant ligand bound to Fe.

The electronic structure and coordination geometry of the Fe atoms in the NFLG as compared to the Fe/NFLG is analyzed by means of Fe K edge XANES and EXAFS spectroscopy. The positions of the absorption pre-edge (1*s* → 3*d* transition) and edge (1*s* → 4*p* transition) resonances in Fig. 1a are an indication of the Fe oxidation state whereas the intensity is lower the higher the symmetry of the Fe sites. The ligand field split pre-edge and the edge appear for the Fe/NFLG at ca. 7114.5–7115.5 eV and 7125 eV respectively, consistent with Fe(III) species as in Fe_2O_3 (orange spectrum), and ferrihydrite *Fh*-FeOOH (green spectrum). The pre-edge intensity of Fe/NFLG is also very similar to Fe_2O_3 indicating a predominant octahedral geometry as opposed to references *Fh*-FeOOH and Fe_3O_4, which also contain tetrahedral sites. In comparison with the references, the more intense while line indicates a more distorted bulk structure or molecular species. In comparison, NFLG is a mixture of metallic Fe and Fe(III) species as shown by the intense shoulder around 7114–7115 eV.

The Fourier transform of the extended X-ray absorption fine structure (FT-EXAFS) spectrum in Fig. 1b shows that the coordination geometry of the scattering Fe in these samples is very different, with the NFLG containing also Fe–Fe distances (corresponding non-phase corrected peak at 2.2 Å) typical of metallic systems, consistent with the XANES data. Metallic species were found coexisting with FeN_4 single sites also in single atoms Fe–N–C systems obtained via various bottom up approaches starting from molecular and polymeric precursors [27].

FT EXAFS data for Fe/NFLG (Fig. 1c) were fitted using two Fe-ligand paths, corresponding to Fe–O(N, C) of different bond length for first shell (non-phase corrected peaks at 1.5 and 1.7 Å), and two Fe-Fe paths with different bond lengths for the second shell. The first peak at ca. 2.6 Å (corresponding to a bond length of 3 Å) is consistent with the edge sharing Fe–Fe distance in lepidocrocite [31] whereas the second non-phase corrected peak at ca. 3 Å (corresponding to a bond length of 3.3 Å) is consistent with corner sharing Fe-Fe distance in ferrihydrite [32]. Fe K-edge FT-EXAFS structural parameters derived from the fits of the samples investigated are summarized in Table S2.

Lepidocrocite is a layered Fe oxy-hydroxide, in which the Fe–O octahedra shares edges forming two dimensional domains. The observation of corner sharing implies that to a certain extent $Fe–L_6$ octahedra develop in this system in three dimensions. It is difficult to conclude from EXAFS whether a direct Fe–C or Fe–N coordination with the support exists. The two different bond lengths might not be necessary due to a different ligand but to some distortion of the Fe–O octahedra. We have determined the N speciation on Fe-NFLG at room temperature and in UHV by means of XPS at the N 1*s* core level as reported in Fig. S1. The fitting of the N 1*s* core level using the model in Refs. [8,14] indicates the presence of a component at a binding energy (BE) of 398.4 eV (N1) attributed to uncoordinated pyridine-like N and a component at a BE of

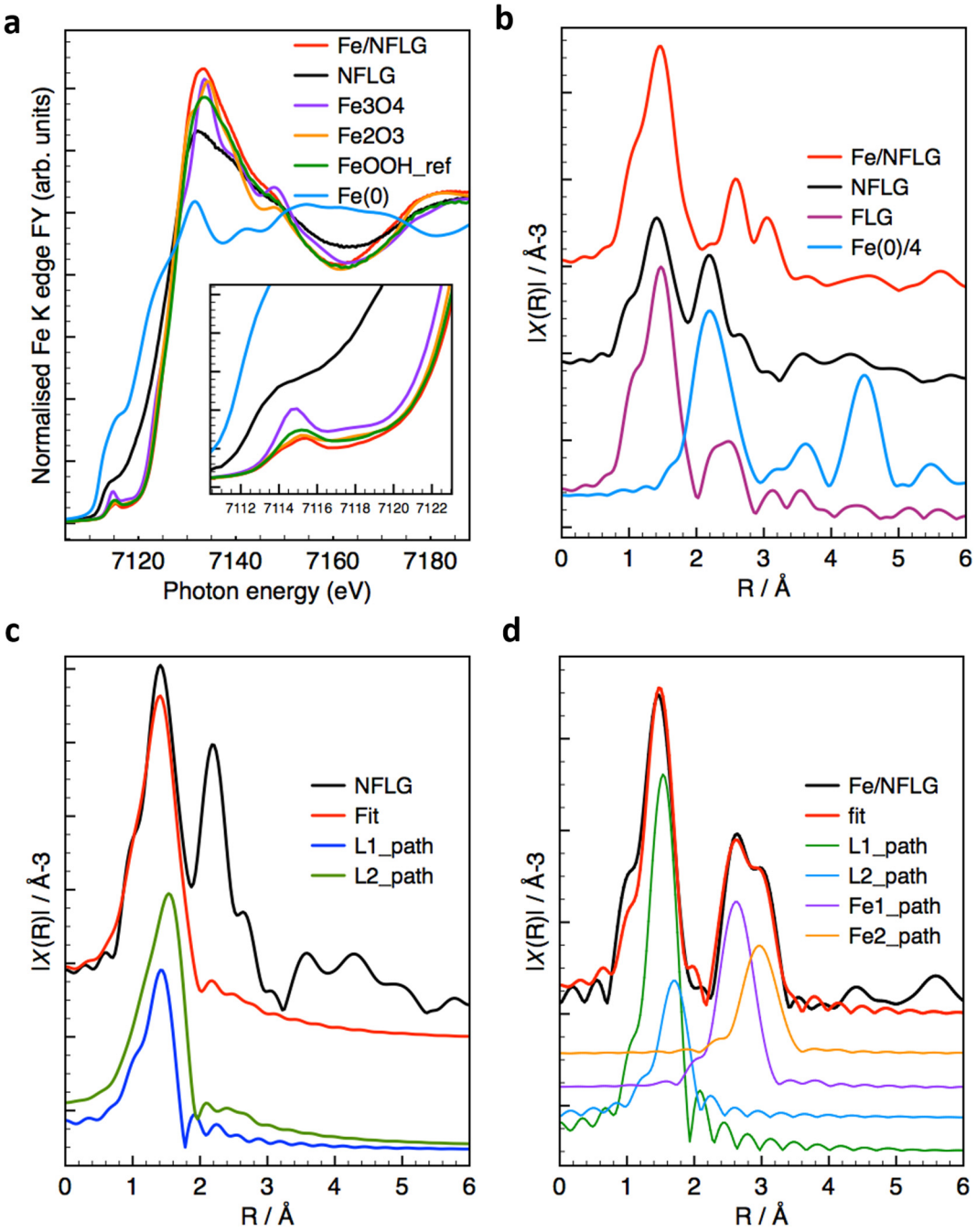

Fig. 1. (a) Fluorescence Yield (FY) Fe K edge XANES spectra of NFLG (black line) and Fe/NFLG (red line) in comparison with Fe_2O_3, Fe_3O_4, Fe metal and *Fh*-FeOOH from Ref. [17]. (b) Non phase-corrected k^2 weighted Fourier transform EXAFS spectra of NFLG and Fe/NFLG and references used for the fitting. (c) Fe/N-C at OCP in 0.05 M $KHCO_3$ (red line). (c) Fit of the Fourier transform EXAFS spectra of NFLG and scattering paths of the first coordination shell obtained from the fitting of FLG in (b). (d) Fit of the Fourier transform EXAFS spectra of Fe/NFLG and scattering paths of the first coordination shell L1 and L2 and 2nd coordination shell Fe1 and Fe2 obtained fromlepidocrocite (database_code_amcsd 0020687) [31] and Fh-FeOOH (PDF 00-058-0898) .cif [32], respectively.

399.9 eV (N2). Uncoordinated pyrrole-like N species are found at a BE half eV higher than 399.9 eV [8,27,28,14] whereas Fe-coordinated pyridine N species are found at a BE half eV lower [8,17]. However, Fe–N bonds were also associated to a component at this BE [27]. We suggest that Fe coordinated to pyrrole-like N is found at a BE similar to uncoordinated pyrrole-like species. Although the spectrum is very noisy a minor component at 401.7 eV (N3) is also visible, which is attributed to quaternary N whose presence is expected considering the synthetic procedure used for obtaining NFLG [28]. XPS did not provide clear evidence for the existence of Fe bound to pyridine-like species. Several reasons could explain this observation, including the possibility that the amount is very low and contributing to the N2 component or that Fe is only coordinated to pyrrole-like species. We do not exclude that the Fe-pyridine species are found underneath oligomeric Fe oxyhydroxide species and therefore not probed due to the surface sensitivity of these measurements. We note that this is also plausible since the Fe speciation indicates that not only ionic

exchange of Fe occurs during this preparation but also precipitation via olation and oxolation triggered by the increase of the local pH at the pyridine N sites.

The fit of the non-metallic component in the NFLG sample in Fig. 1d is challenging due to the presence of the metallic phase. However, the fit parameters obtained for FLG (purple line in Fig. 1b), which contains only a non-metallic phase, describe very well also the non-metallic phase in NFLG. The fit considers two paths, L1-path and L2 path corresponding to the peaks at 1.4 Å and 1.54 Å (non-phase corrected), respectively, which are slightly shorter than the Fe-L distances in Fe/NFLG. Also, in this case, the fitting reveals a 6-coordination, consistent with Fe in distorted octahedral geometry. Such coordination geometry was found for FeN_4 ensembles in Fe–N–C by means of electron paramagnetic resonance spectroscopy [27]. The electron microscopy analysis of this sample will clarify the nature of these species as single Fe atoms coordinated to terminal atoms of the graphene layers. It is worth noting that although the position of the edge and the white line shape for NFLG (Fig. 1a) are well reproduced by linear combination fitting using a Fe foil as reference for metallic Fe sites, the features after the edge were not well fitted. Consistently in Fig. 1b, the peak at 4.5 Å (non-phase corrected) typical for bulk Fe is not observed for NFLG suggesting that the Fe metallic phase in this sample is composed of few atom metallic clusters.

3.2. Defects on N-doped graphene during annealing

To identify the nature and the thermal stability of defects in NFLG, HAADF-STEM (Fig. 2) is carried out during a thermal annealing in ultra-high vacuum (UHV) conditions. In order to stay below the knock-on damage threshold for carbon, the imaging measurements were performed at 80 keV acceleration voltage and an electron dose as low as ~10^3 e^- nm^{-2} s^{-1}, which is significantly lower than electron doses commonly used for imaging. This proved to be sufficiently low to prevent beam induced effects, consistently with literature findings [24].

NFLG has no visible non-6-membered in-plane defects. The variation in contrast in the in-plane area (Fig. 2a) is due to a variation of thickness: a darker area indicates fewer graphene layers stacking on top of each other and *vice versa*. The shape of the top-most graphene layers can be understood from the edges of the graphene layers which appear brighter. Other larger brighter areas in Fig. 2a could be due to quasi 1D graphene nanoribbons which are expected to be found in graphene oxide [33]. Few visible heavier single atoms are in this area, at the trim of the graphene layers (Fig. 2a) and in in-plane positions (Fig. 2b–d), and account for the metal impurities existing in the starting material, consistent with the EDX analysis in Table S1. Considering the brightness of these atoms and the XAS analysis for this sample, we postulate that these are Fe atoms. As presented above, Fe exists in this sample as isolated Fe(III) species in distorted octahedral geometry and metallic few Fe atoms clusters. We will discuss the coordination geometry of Fe species and their dynamics in detail for Fe/NFLG in the next section. For NFLG, the most evident structural modification occurring due to the thermal annealing is the variation of the geometric configuration at the trims of the several graphene layers stacking on top of each other. This clearly indicates a rearrangement of edge bonds via bond breaking and making. A closer inspection of the edges of the starting material at room temperature (Fig. 2a and inset) indicates that NFLG is characterized by a mixture of zig-zag and armchair sites. For example, these zig-zag terminations are three hexagon long in 2a and 2b and corresponding 1 and 2 insets. Of interest for chemical reactivity, the zigzag edges present nonbonding π-electron state available for interaction with host species and are commonly found in graphene oxide together with in-plane oxygen defects [33,34]. Substitutional N-

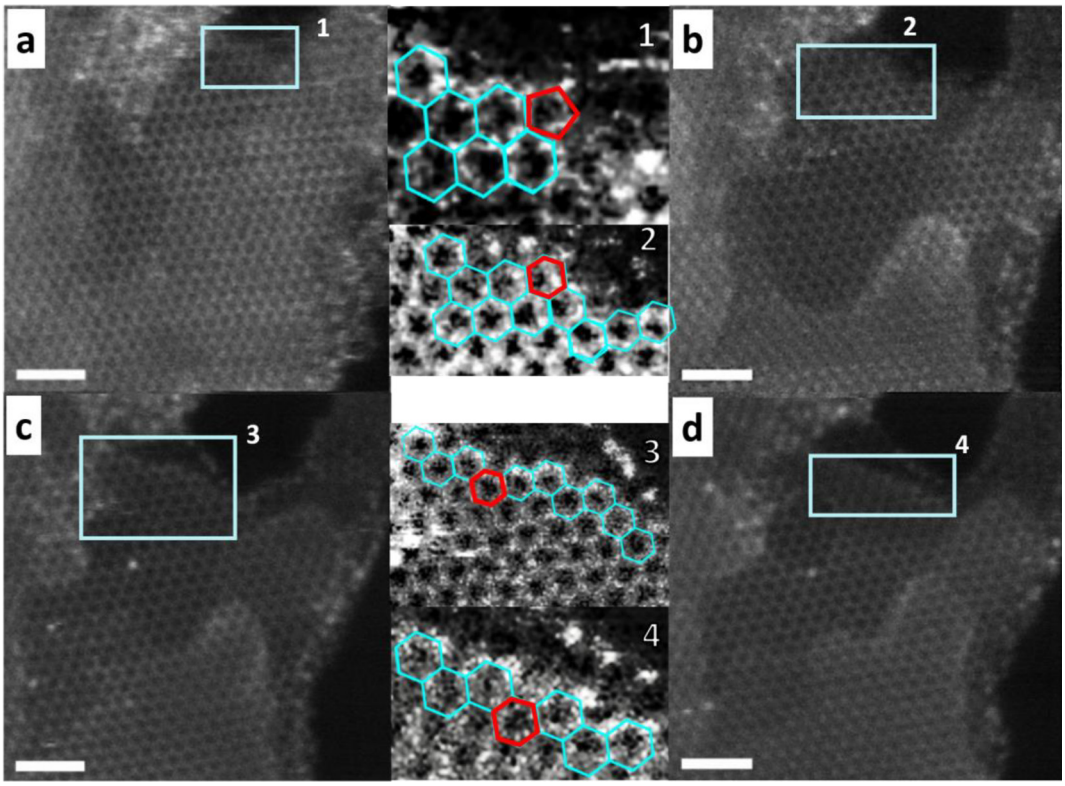

Fig. 2. Topological evolution of NFLG at (a) room temperature, (b) 773 K, (c) 973 K, and (d) 1073 K. Detail of the graphene edge and superimposed graphene model in the inset as indicated in the labels. The red pentagon and hexagons are included as a guidance for the edge rearrangement. The scalebar is 1 nm; Gaussian blur: 1.5.

heteroatoms in graphene produce charge localization that would be also stabilized at zig-zag termination being these characterized by edges states as opposed to armchair sides in which edge states are absent [33].

Koskinen et al. [34] has shown that the mixed terminations seen in the starting material also accommodate non-6 membered rings at the junction between one edge type and the other. Indeed, the contrast variation within area 1 in Fig. 2a and related inset would be better described by the presence of a pentagonal ring at the edge termination. Therefore, these defects at the edges cannot be excluded here and would explain the easy transformation of the edges upon thermal treatment into more stable 6-membered rings. These sites might also accommodate the N atom in pyrrole-like configuration. When subjected to Fe ionic exchange in solution, Fe atoms can coordinate to these sites, consistent with the N 1*s* XPS analysis (Fig. S1).

The most pronounced structural modification occurs however at high temperature as shown by the changes in the shape of the graphene top-most layers (Fig. 2b–d) when compared with the starting material (Fig. 2a). The edges appear more defined at 973 K and a conversion to form an armchair termination configuration is seen (Fig. 2c and inset 3). This transformation can be explained in terms of a large aromatic stability in the armchair edge [33], with the consequence that the edges of this material are less reactive.

With increasing the temperature, the conversion of the edge into an armchair configuration progresses further (Fig. 2d and inset 4).

However, we should point out that the sample is still characterized by graphene termination with a mixture of armchair and zig-zag configurations.

The false images of the HAADF-STEM in Fig. 3 evidence the modifications of the trims of the graphene layer occurring between 973 K and 1073 K as well the more intense contrast of the atoms there, suggesting either that these might have a higher atomic number than C, but much lower than the single atom impurities present on this sample, or localized charge accumulation. The arrow in Fig. 3a addresses a metal atom which has moved away from the original position (Fig. 3b). It will be shown later on that especially at these high temperatures, Fe atoms interact with the trims of the graphene layers producing enlargement of holes or reduction of the dimension of the graphene patches.

3.3. Dynamics of Fe species on N-doped graphene during annealing

The low magnification bright field image of Fe/NFLG measured at 373 K is reported in Fig. 4a. The image recorded on the same area after the *in situ* annealing experiments is shown in Fig. 4b. In the latter image, the formation of large particles appearing as dark spots, which are not observed in the sample at 373 K (Fig. 4a), allow us to conclude that the immobilized Fe species underwent a dramatic sintering process upon annealing.

To better clarify the timescale of the dynamics occurring on this sample, Fig. S2 shows a sequence of images recorded during a temperature programmed experiment over Fe-NFLG. A video relative to this figure is included as Supporting Video file 1. We can identify

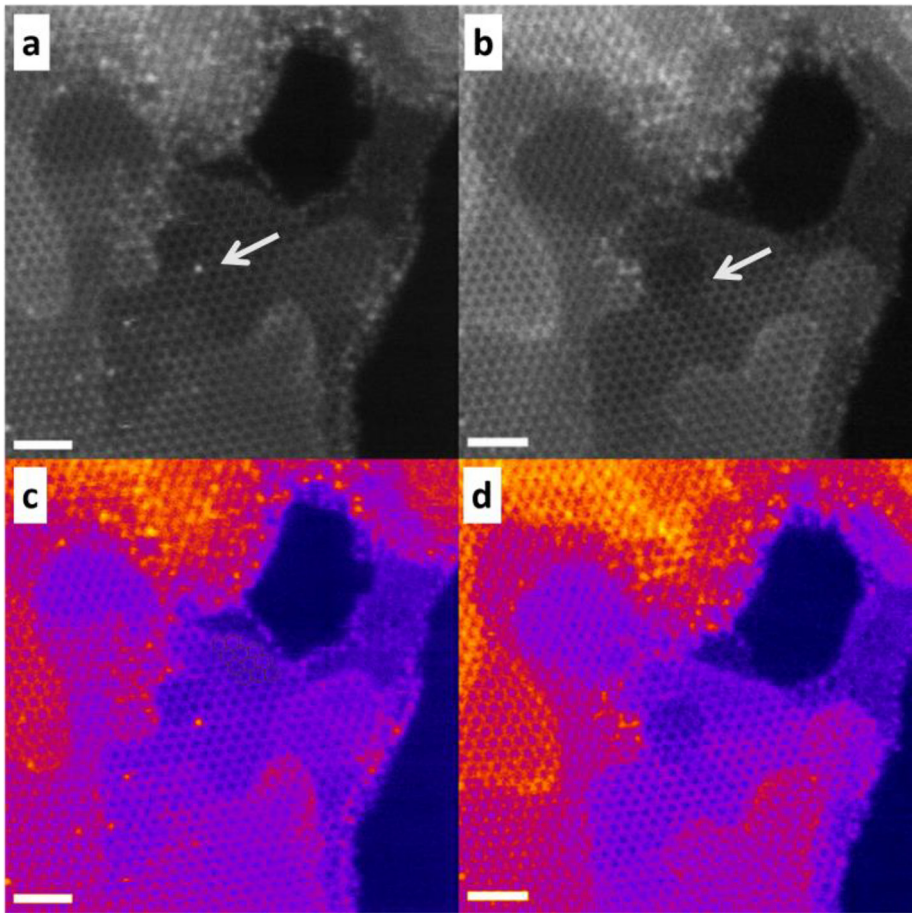

Fig. 3. Topology evolution on few layers N-doped graphene during thermal treatment. HAADF-STEM at (a) 973 K and (b) 1073 K. Corresponding false image at (c) 973 K and (d) 1073 K. The scalebar is 1 nm; Gaussian blur: 1.5.

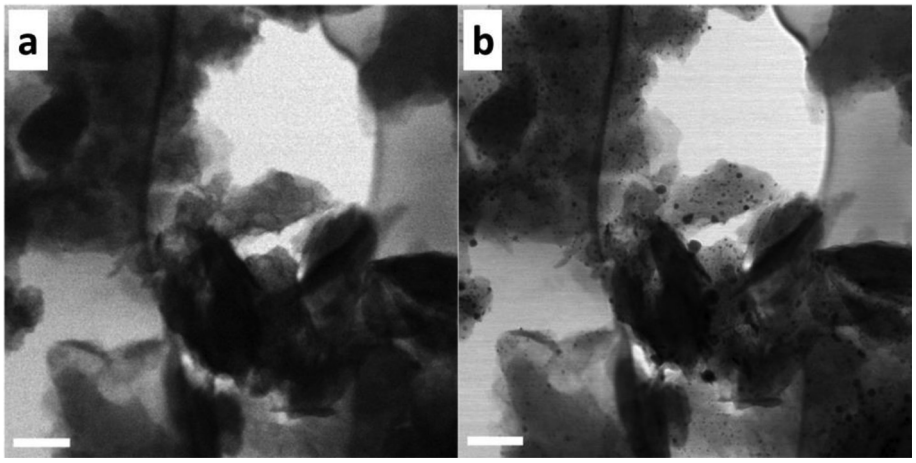

Fig. 4. Overview BF-STEM images at 373 K (a) vs 973 K (b). Scalebar: 300 nm.

three temperature ranges characterized by specific Fe dynamics: at temperature below 573 K the main transformation involves the diffusion of Fe atoms along the trims of the graphene layers; above this temperature, the diffusion of Fe atoms from the edges toward an in-plane position begins to occur; above 1073 K, the dynamics are very drastic and involve the etching of the graphene edges by the Fe atoms localized at the edges (Fig. S3 and Supporting Video file 2). At this temperature, single atoms are also found in-plane positions as well at the graphene edges.

Fig. 5 shows the localization of Fe atoms at the different temperatures. Below 573 K Fe atoms (brighter spots) in close proximity to each other are localized mainly at the graphene edges (Fig. 5a), consistent with previous finding [35], and as expected if no in-plane defects are presents in graphene. Upon annealing above 573 K the Fe atoms diffuse towards the inner region of the graphene layer (Fig. 5b). However above 973 K, we also find that the in-plane Fe sites have reduced the perimeter of the graphene layers (Fig. 5c) ultimately leading to the extensive Fe sintering observed in the low magnification TEM image in Fig. 4b. Previous work has shown that Fe atoms trapped in beam induced monovacancy are also susceptible of beam induced diffusion via bond breaking, C atom emission and rearrangement [37]. Our results show that a similar dynamic interconversion occurs but, in our experiments, this is due thermal activation.

We now analyze the structural configurations of the isolated Fe species in this sample and evaluate the extent of any beam effect. Fig. 6 shows two pictures taken at 973 K and at different time in an adjacent area, which includes a region of the sample not previously irradiated. We can see a large population of isolated single Fe atoms in three-coordinated or four-coordinated Fe sites resembling porphyrin-like metal center. This confirms the high thermal stability of the few in-plane, three and four coordinated single

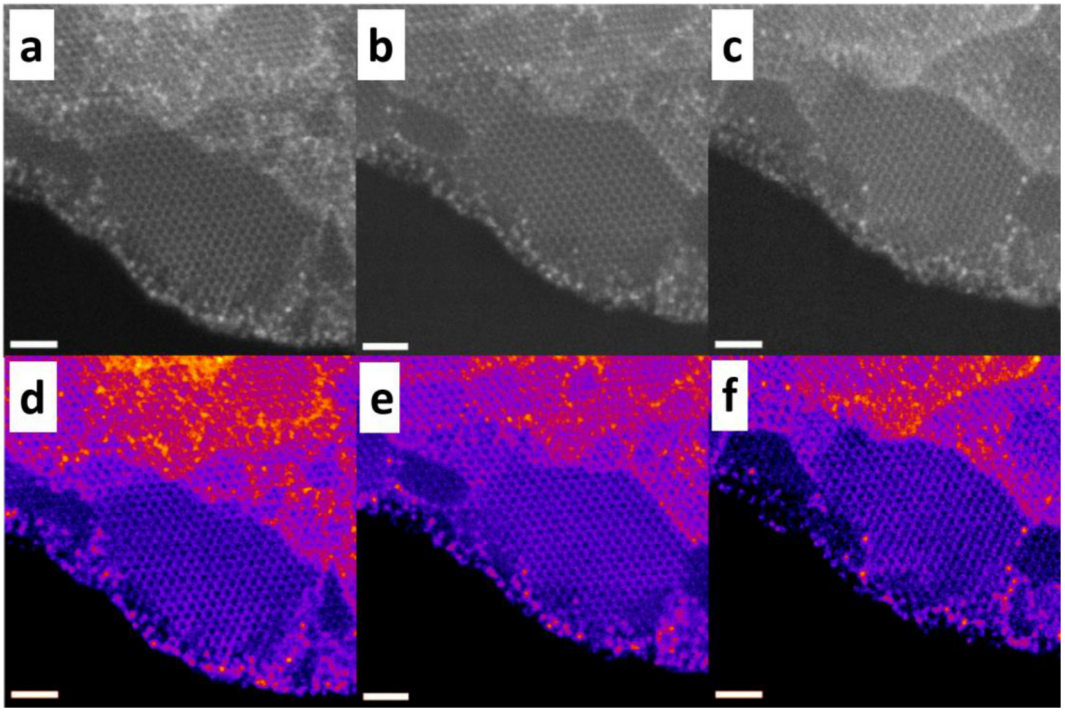

Fig. 5. Topology evolution on few layers Fe-N-doped graphene at (a) 573 K (b) 773 K and (c) 973 K; and corresponding false image in (d), (e) and (f), respectively. The scalebar is 1 nm; Gaussian blur: 1.5.

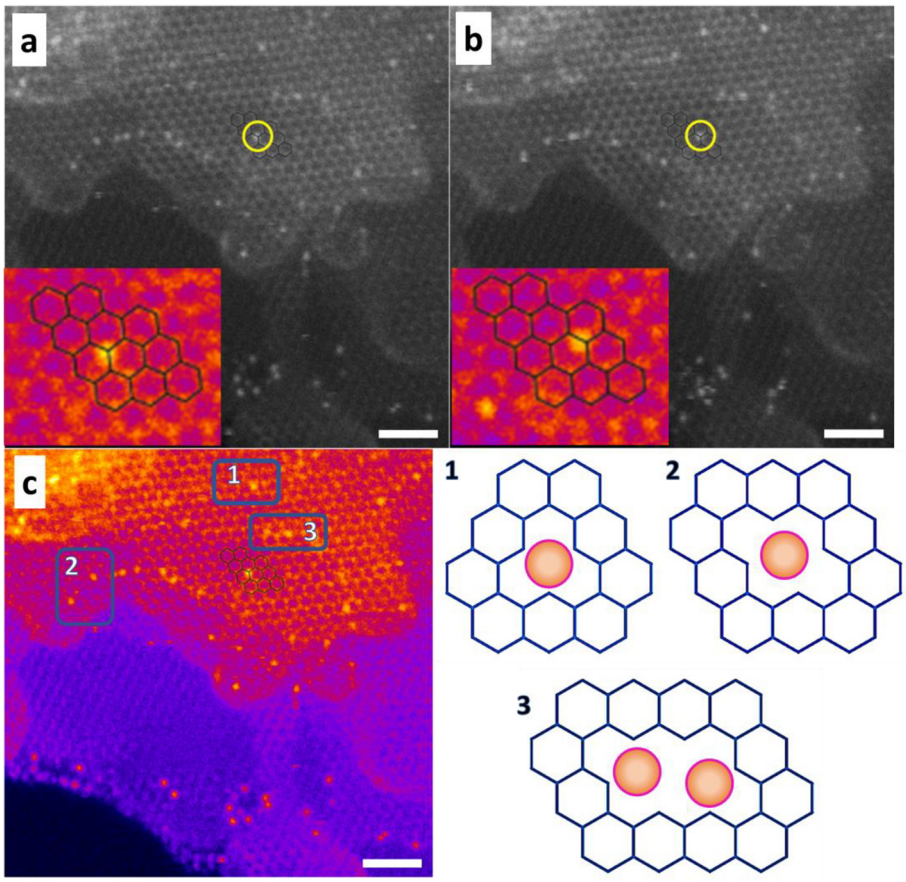

Fig. 6. Topological evolution on few layers Fe-N-doped graphene at 973 K at different time. The insets show the motion of the metal atoms from the center of the vacancy (a) towards an edge side of the vacancy (b). (c) Structure of Fe species: three-coordinated Fe (1); four-coordinated Fe (2); dinuclear Fe species (3). Scalebar: 1 nm.

atom sites formed. This is in contrast with the Fe atoms at the edges which are not as stable and diffuse fast at lower T (Video 1), consistent with previous consideration that the stability of single Fe atoms is higher the higher the number of atoms coordinated to it [37]. Moreover, the three-coordinated Fe atoms appear to be central with respect to the single vacancy in Fig. 6a (inset) and between two C atoms of the graphene lattice in Fig. 6b (inset). Whilst for Fe atoms trapped in monovacancies, it is expected that the Fe atom is localized out of plane and central to the vacancy, Fe atoms between two C atoms were also reported and explained in terms of the defect being captured between two states, with the Fe atom oscillating between two positions [24]. This explanation is plausible also for our results, indicating a beam effect occurring in a time frame of 50 s, which is however much longer than

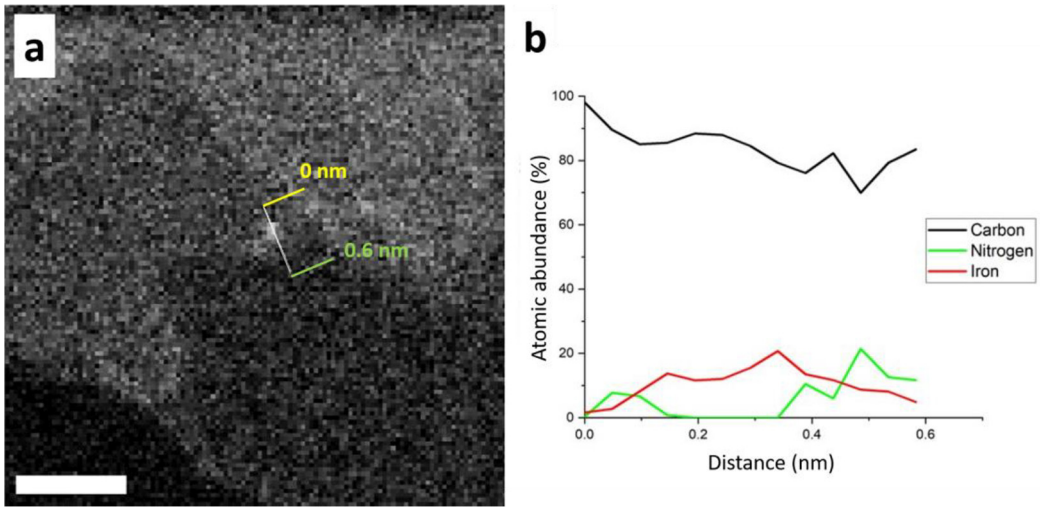

Fig. 7. (a) HAADF-STEM of Fe-NFLG at 873 K showing a single Fe atom and the position of the EELS line scan. (b) Evolution of the atomic abundance of the elements obtained from EELS quantitative analysis as a function of distance as indicated. Scale bar: 1 nm.

reported in the literature [24]. This is the only evidence of beam effect observed during our study, although one should also point out that such vibrations could be due to thermal activation as well.

Fig. 6c clarifies the different type of Fe sites observed at high temperature. We can distinguish three-coordinated Fe, four-coordinated Fe sites and di-nuclear Fe sites. We hypothesize that these Fe sites manifesting high thermal stability are coordinated to N-atoms. Whilst N 1*s* XPS (Fig. S1) confirmed the presence of various N species, the localization of Fe and N atoms remains unclear.

We further carried out the local elemental analysis on Fe/NFLG by means of atomic resolved EELS. A line scan across a single metal site is reported in Fig. 7. The evolution of the C, N, and Fe abundances in atomic percent across this line is shown in Fig. 7b, indicating that at least two N atoms at the edge of the vacancy coordinate the Fe metal atom. We note that the nature of the bonding between Fe and N in these systems is still an active discussion in the literature: both Fe-pyrrole and Fe-pyridine coordinations are options for Fe-N_4 species whereas for three coordinated Fe-N_3 sites, a pyridine coordination to Fe is more plausible. Ni et al. have shown that for penta-coordinated FeN_4 species in carbon materials, bond lengths for pyridine coordination are systematically shorter (1.946–1.931 Å) than for pyrrolic coordination (2.007–2.012 Å) [27]. If we consider that the Fe single sites observed on NFLG are likely of the same nature as those formed on Fe/NFLG during the in situ annealing, from Table S2 we can infer that approximately two bonds of length 1.904 Å are related to Fe-pyridine whereas the other 4 bonds of length 2.077 Å are due to Fe-C or axial Fe (III)-OH_2 [36], consistent with the longer bond found for N-free FLG.

The line scan across a highly defective area formed at 873 K where many Fe atoms are located (Fig. 8a) confirms the presence of N species in the same location of Fe atoms (Fig. 8b). The intensities of the N K end Fe L edges however change in the different

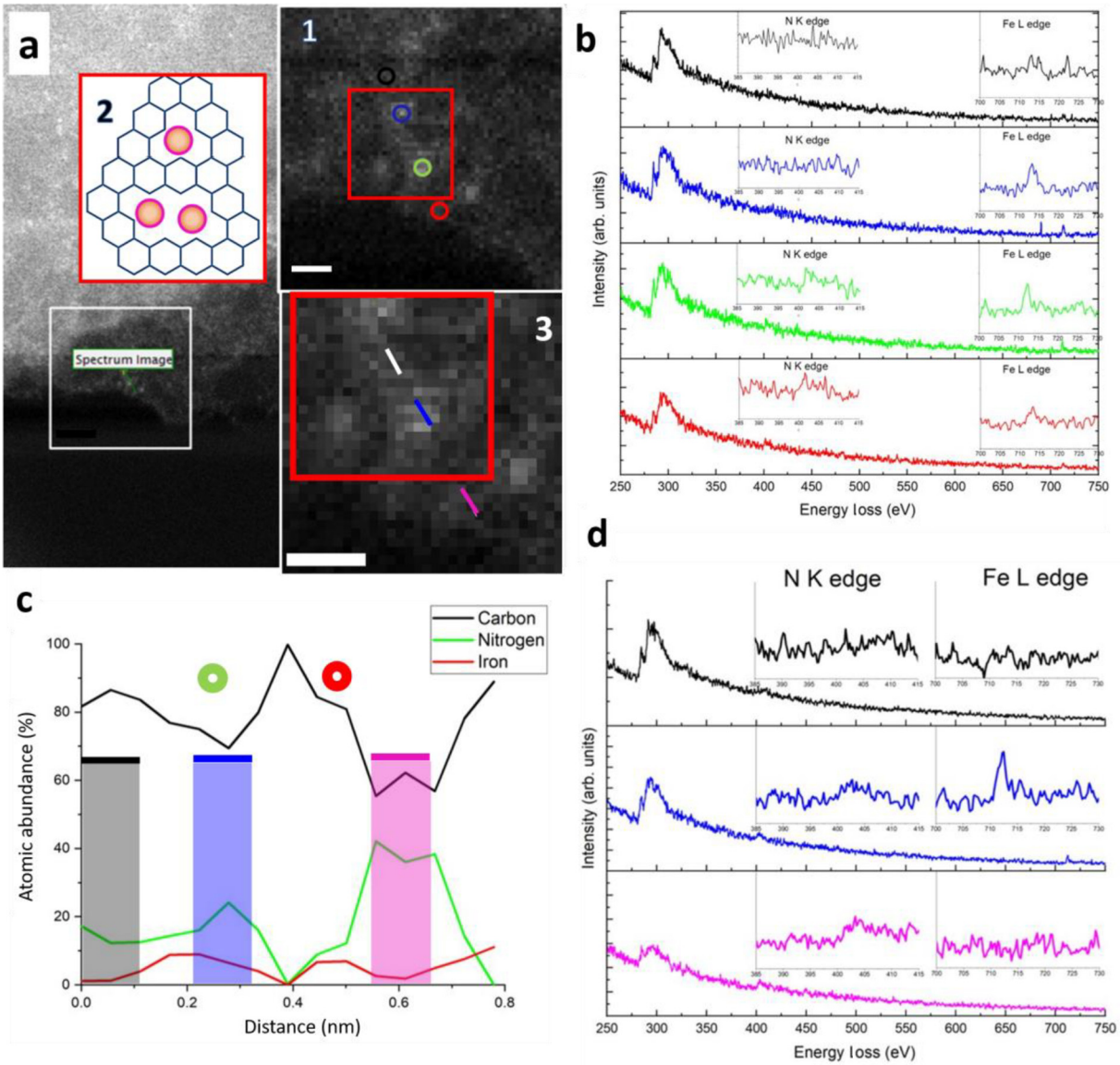

Fig. 8. HAADF-STEM of Fe-NFLG at 873 K (a) with indication of the points at which EELS spectra with 1 pixel resolution (0.056 nm) were recorded (inset 1) and constructed model of Fe ensemble (inset 2) assuming the closest Fe–Fe distance as in the dinuclear site of Fig. 6c, inset 3. (b) Corresponding EELS spectra with 1 pixel step size (0.056 nm) where the color is consistent with the colors assigned to each position in the inset 1. (c) Atomic abundance of the elements as a function of the distance in the line scan with color and shape coded indication of the positions of measurements. (d) Corresponding EELS spectra with 2 pixels step size (0.11 nm) where the color is consistent with the colors assigned to each position in inset 3. Scale bar: 0.3 nm.

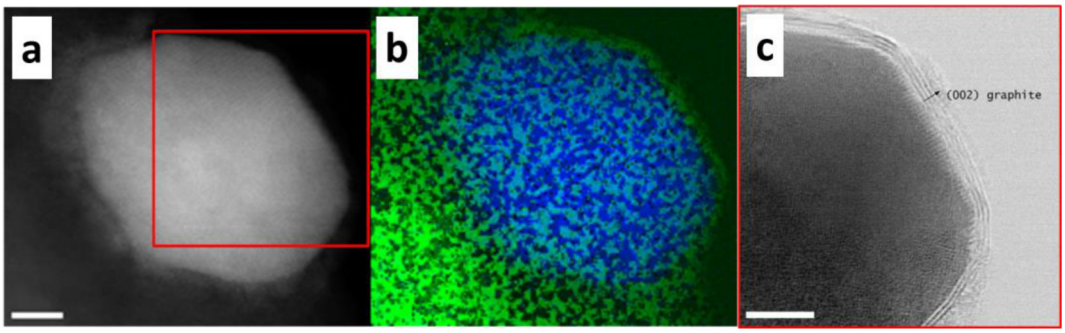

Fig. 9. STEM SI EELS analysis. (a) ADF STEM, (b) overlay of extracted Fe L (blue) and C K (green) edge SI signal map from area (a). (c) BF STEM image relative to the area within the red rectangle in (a). d-spacing = 0.338 nm; scalebar: 5 nm.

spots: particularly the blue spot centered on the bright region is rather N-free. In contrast, the presence of N is evident at the green and red spots (Fig. 8b).

Due to the small pixel size used to collect the EELS signal in Fig. 8b the spectrum for N is very noisy. We show the quantitative analysis obtained integrating 2 pixels size in Fig. 8c and the corresponding EELS spectra in Fig. 8d. As expected, the signal is now improved and enable us to evaluate the energy loss position and the shape of the N K edge as well as the Fe L edge and extract analytical information. Accordingly, the Fe L edge position at 712.5 eV indicates Fe(III) species. No resonances related to the OK edge are observed (Fig. 8b and d) and therefore it is correct to infer that C and N are coordinated to the Fe(III) species. In the case of the N K edge, the onset of the signal is at 400 eV and the maximum of the σ^* resonance is at 404 eV, whereas no clear sharp π^* resonance due to C═N bonds is observed. Similar N K edge spectra were obtained by Chung et al [38] for Fe–N–C systems obtained via bottom-up approaches and attributed to Fe–N_4 ensembles. A similar N K edge EELS spectrum was found for N-functionalized carbon nanotube with similar amount of pyrrolic and pyridine N as opposed to pyridine enriched carbon nanotube which shows a more intense π^* resonance [5]. This suggest that most probably both coordination environments exist.

The elemental composition in atomic percent for the overall area of the ensemble is C 71 ±3%; N 24.1 ±0.9%; Fe 4.49 ±0.17% with a N/Fe ratio of 5.36. The higher amount of N with respect to Fe indicates a multiple N-coordination however with some deviation from the Fe-N_4 case. The evolution of the elementś abundances for this type of site (Fig. 8c) shows area of high N content (from 0.4 nm to 0.6 nm the N/Fe ration is 4) and area of lower N content (from 0.4 nm to 0.2 nm the N/Fe ration is 2); moreover, there are regions in which no N is present (blue spectrum in Fig. 8b), suggesting a direct Fe–C coordination. The Fe–C bond is weaker that the Fe–N bond and this can induce a higher mobility of the Fe atoms and explain the formation of polynuclear Fe ensembles.

A model of this dinuclear ensemble is shown in the inset 2 of Fig. 8a. Recently Chen et al. [39], have indicated bimetallic graphene nitrene heterostructure FeFe–grafiN_6 systems as active sites for CO_2 reduction to multi-carbon products. The existence of this type of sites is also supported by our TEM analysis. The distance between the Fe atoms in the di-nuclear complex in Fig. 6 and Fig. 8 is 3.2 nm, similar to the diiron distance in monooxygenase model complexes [40]. However, the presence of N-free Fe–C ensembles leads to the formation of instable dinuclear Fe specie which lead to the formation of metal cluster as indicated by XAFS analysis (Fig. 1a and d) with time through a mechanism of C–C bond breaking and making (Fig. S3 and Video 2) and potentially gasification [37] via by Fe–C bond formation. In the case of high loaded samples such as Fe/NFLG, large Fe nanoparticles are formed.

Fig. 9 reports the characterization of the big Fe particles after the *in situ* annealing to 1073 K. STEM-EELS maps were acquired to determine the elemental composition and revealed that the Fe particles are composed of a Fe metallic core and an oxide layer and covered by a carbon overlayer (Fig. 9a and b. The particles are composed of a Fe metallic core and an oxide layer. Interestingly we found that the particles are covered by few graphene layers (Fig. 9c) revealing a d-spacing of 0.338 nm in agreement with the (0 0 2) planes of graphite. This indicates that the original graphene support was consumed to growth secondary layers when the sintered particles were formed. This is expected considering that Fe is known to grow carbon nanotubes at temperature above 873 K [41].

No evidence of a stable carbide phase was observed; however, the presence of the graphene layer indicates the *in situ* formation of a metastable carbide phase which segregated graphene layers upon cooling.

4. Conclusions

In this work we show that in-plane defect-free, N-doped few layer graphene is characterized by dynamics occurring only upon thermal annealing at relatively high temperature. The observed dynamics consist of edges rearrangements to form more stable edge terminations in the armchair configuration, triggered by the existence of edge defects such as pentagonal rings. The adsorption of Fe species from an aqueous solution leads the edge of this N-doped graphene to be decorated by Fe atoms in close proximity with each other. These are octahedral Fe(III) species in polynuclear oxyhydroxide disordered nanostructures. The thermal annealing favors first the fast diffusion of these Fe atoms at the edges of the graphene layers (below 573 K), and at higher T the in-plane migration of these Fe atoms is observed to form very stable four-coordinated and three-coordinated Fe- single atomic species together with dinuclear Fe species within a more complex ensemble closer to the edge of the graphene layer. However, not all the Fe atoms initially present are stabilized by the interaction with graphene. The diffusion of the Fe atoms from one site to the other at the trim of the graphene layers is very rapid leading to the formation of Fe agglomerates. At very high temperature the breaking of the C-C bonds at the edges of the graphene layer by the metal atoms causes also sintering of the metal species to form Fe NPs. This mechanism ultimately leads to the segregation and precipitation of graphitic C from the sintered metallic particle, probably upon cooling down during the *in situ* experiment. We postulate that the interaction of Fe with a C–H termination of the graphene later might lead to this phenomenon whereas the presence of N stabilizes the edges and warrants the stability of the Fe–N ensem-

bles even at higher temperature. We also note that the few metal Fe impurities existing on the NFLG have undergone similar dynamics during the synthesis step resulting in the formation of small metallic clusters and isolated Fe species in octahedral coordination under atmospheric conditions of XAFS measurements. Due to lower Fe loading of this sample compared to Fe/NFLG, larger Fe particles are not formed. Our results show the high dynamic character of Fe species in Fe N-doped graphene-based systems and corroborate the hypothesis that the catalytic performance might not be due to single atom sites but more complex species, whose reactivity depends on the structural details of the surrounding graphitic environment in which these are formed. These polynuclear models could explain the C–C coupling reactivity showed by Fe–N–C systems in multielectron transfer reactions.

Declaration of Competing Interest

The authors declare that they have no known competing financial interests or personal relationships that could have appeared to influence the work reported in this paper.

Acknowledgments

R.A. acknowledges The UK Catalysis Hub for support provided via the membership of the UK Catalysis Hub Consortium and funded by EPSRC (portfolio grants EP/K014706/1, EP/K014668/1, EP/K014854/1, EP/K014714/1 and EP/I019693/1). We thank Diamond Light Source for beamtime (SP17031).

Appendix A. Supplementary data

Supplementary data to this article can be found online at https://doi.org/10.1016/j.jechem.2021.05.005.

References

[1] Y. Lin, X. Sun, D.-S. Su, G. Centi, S. Perathoner, Chem. Soc. Rev. 47 (2018) 8438–8473.
[2] H.J. Choi, J. Ihm, S.G. Louie, M.L. Cohen, Phys. Rev. Lett. 84 (2000) 2917–2920.
[3] W. Qi, W. Liu, B. Zhang, X. Gu, X. Guo, D.-S. Su, Angew. Chem. Int. Ed. 52 (2013) 14224–14228.
[4] K.F. Ortega, R. Arrigo, B. Frank, R. Schlögl, A. Trunschke, Chem. Mater. 28 (2016) 6826–6839.
[5] R. Arrigo, M.E. Schuster, Z. Xie, Y. Yi, G. Wowsnick, L.L. Sun, K.E. Hermann, M. Friedrich, P. Kast, M. Hävecker, A. Knop-Gericke, R. Schlögl, ACS Catal. 5 (2015) 2740–2753.
[6] H. Ba, C. Duong-Viet, Y. Liu, J.-M. Nhut, P. Granger, M.J. Ledoux, C. Pham-Huu, C. R. Chim. 19 (2016) 1303–1309.
[7] Y. Lin, Z. Liu, Y. Niu, B. Zhang, Q. Lu, S. Wu, G. Centi, S. Perathoner, S. Heumann, L. Yu, D.-S. Su, ACS Nano 13 (2019) 13995–14004.
[8] R. Arrigo, M.E. Schuster, Catalysts 9 (2019) 303.
[9] S. Chen, S. Perathoner, C. Ampelli, C. Mebrahtu, D. Su, G. Centi, ACS Sustainable Chem. Eng. 5 (2017) 7393–7400.
[10] R. Arrigo, M.E. Schuster, S. Abate, G. Giorgianni, G. Centi, S. Perathoner, S. Wrabetz, V. Pfeifer, M. Antonietti, R. Schlögl, ACS Catal. 6 (2016) 6959–6966.
[11] C.I. Gerber, P. Serp, Chem. Rev. 120 (2020) 1250–1349.
[12] R. Arrigo, M. Haevecker, R. Schloegl, D.-S. Su, Chem. Commun. (2008) 4891–4893.
[13] R. Arrigo, S. Wrabetz, M.E. Schuster, D. Wang, A. Villa, D. Rosenthal, F. Girsgdies, G. Weinberg, L. Prati, R. Schloegl, D.-S. Su, Phys. Chem. Chem. Phys. 14 (2012) 10523–10532.
[14] A.I. Large, S. Wahl, S. Abate, I. da Silva, J.J. Delgado Jaen, N. Pinna, G. Held, R. Arrigo, Catalysts 10 (2020) 1289.
[15] A. Li, S.A. Nicolae, M. Qiao, K. Preuss, P.A. Szilgyi, A. Moores, M.-M. Titirici, ChemCatChem 11 (2019) 3602.
[16] A.S. Varela, W. Ju, P. Strasser, Adv. Energy Mater. 8 (2018) 1703614.
[17] C. Genovese, M.E. Schuster, E.K. Gibson, D. Gianolio, V. Posligua, R. Grau-Crespo, G. Cibin, P.P. Wells, D. Garai, V. Solokha, S. Krick Calderon, J. Velasco Velez, C. Ampelli, S. Perathoner, G. Held, G. Centi, R. Arrigo, Nat. Commun. 9 (2018) 935.
[18] S. Chen, S. Perathoner, C. Ampelli, H. Wei, S. Abate, B. Zhang, G. Centi, J. Energy Chem. 49 (2020) 22–32.
[19] H. Guo, M. Li, X. Liu, C. Meng, R. Linguerri, Y. Han, G. Chambaud, Catal. Sci. Technol. 7 (2017) 2012–2021.
[20] J.M. Thomas, Nat. Catal. 525 (2015) 325–326.
[21] A. Wang, J. Li, T. Zhang, Nat. Rev. Chem. 2 (2018) 65–81.
[22] G.S. Parkinson, Catal. Lett. 149 (2019) 1137–1146.
[23] R. Gusmão, M. Vesely, Z. Sofer, ACS Catal. 10 (2020) 9634–9648.
[24] A.W. Robertson, B. Montanari, K. He, J. Kim, C.S. Allen, Y.A. Wu, J. Olivier, J. Neethling, N. Harrison, A.I. Kirkland, J.H. Warner, Nano Lett. 13 (2013) 1468–1475.
[25] A. Robertson, C. Allen, Y. Wu, K. He, J. Olivier, J. Neethling, A.I. Kirkland, J.H. Warner, Nat. Commun. 3 (2012) 1144.
[26] J. Zheng, S. Wu, L. Lu, C. Huang, B. Ho, A. Kirkland, T. Sudmeier, R. Arrigo, D. Gianolio, S. Chi, E. Tsang, Chem. Sci. 12 (2021) 688–695.
[27] L. Ni, C. Gallenkamp, S. Paul, M. Kübler, P. Theis, S. Chabbra, K. Hofmann, E. Bill, A. Schnegg, B. Albert, V. Krewald, U.I. Kramm, Adv. Energy Sustainability Res. 2 (2021) 2000064.
[28] R. Arrigo, M. Haevecker, S. Wrabetz, R. Blume, M. Lerch, J. McGregor, E.P.J. Parrott, J.A. Zeitler, L.F. Gladden, A. Knop-Gericke, R. Schloegl, D.-S. Su, J. Am. Chem. Soc. 132 (2010) 9616–9630.
[29] B. Ravel, M. Newville, J. Synchroton Rad. 12 (2005) 537–541.
[30] G. Held, F. Venturini, D.C. Grinter, P. Ferrer, R. Arrigo, L. Deacon, W. Quevedo Garzon, K. Roy, A. Large, C. Stephens, A. Watts, P. Larkin, M. Hand, H. Wang, L. Pratt, J.J. Mudd, T. Richardson, S. Patel, M. Hillman, S. Scott, J. Synchrotron Rad. 27 (2020) 1153–1166.
[31] A.N. Christensen, M.S. Lehmann, P. Convert, Acta Chem. Scand. A 36 (1982) 303–308.
[32] F.M. Michel, L. Ehm, S.M. Antao, P.L. Lee, P.J. Chupas, G. Liu, D.R. Strongin, M.A. A. Schoonen, B.L. Phillips, J.B. Parise, Science 316 (2007) 1726–1728.
[33] T. Enoki, S. Fujii, K. Takai, Carbon 50 (2012) 3141–3145.
[34] P. Koskinen, S. Malola, H. Häkkinen, Phys. Rev. 80 (2009) 073401.
[35] W. Zhang, L. Sun, Z. Xu, A.V. Krasheninnikov, P. Huai, Z. Zhu, F. Banhart, Phys. Rev. B 81 (2010) 125425.
[36] K. Stone L., K. Behan R., T. Green M., X-ray Absorption Spectroscopy of Chloroperoxidase Compound I: New Insight into the Reactive Intermediate of P450 Chemistry., PNAS 102 (2005) 16563–16565, https://doi.org/10.1073/pnas.0507069102.
[37] A.V. Markevich, M. Baldoni, J.H. Warner, A.I. Kirkland, E. Besley, J. Phys. Chem. C 120 (2016) 21998–22003.
[38] H.T. Chung, D.A. Cullen, D. Higgins, B.T. Sneed, E.F. Holby, K.L. More, P. Zelenay, Science 357 (2017) 479–484.
[39] S. Chen, H. Yuan, S.I. Morozov, L. Ge, L. Li, L. Xu, W.A. Goddard, J. Phys. Chem. Lett. 7 (2020) 2541–2549.
[40] G.E. Cutsail III, R. Banerjee, A. Zhou, L. Que Jr., J.D. Lipscom, S. DeBeer, J. Am. Chem. Soc. 140 (2018) 16807–16820.
[41] A. Rinaldi, J.-P. Tessonnier, M.E. Schuster, R. Blume, F. Girgsdies, Q. Zhang, T. Jacob, S.B. Abd Hamid, D.S. Su, R. Schlögl, Angew. Chem. Int. Ed. 50 (2011) 1–6.